Forward volume wave microwave envelope solitons in yttrium iron garnet films: Propagation, decay, and collision

Mincho A. Tsankov,[a] Ming Chen, and Carl E. Patton
Department of Physics, Colorado State University, Fort Collins, Colorado 80523

(Received 14 March 1994; accepted for publication 24 June 1994)

Magnetostatic forward volume wave (FVW) microwave magnetic envelope solitons in 7.2 μm thick, single-crystal yttrium iron garnet films have been studied at 5.6–6.0 GHz. Rectangular input pulses with peak powers up to 3 W and pulse widths 5–50 ns were used. Single soliton output pulses with a characteristic increase in amplitude and pulse narrowing are observed when the power or width of the rectangular input microwave pulse exceeds threshold levels. Above these levels, output pulse peak power versus input power or pulse width exhibits a nonlinear increase and shows saturation effects. Multiple peak output profiles are observed for pulse powers and widths well above threshold. Solitons could be formed for all frequencies within the usable, low transmission loss portion of the magnetostatic FVW band. The use of reflected pulses from the film edge made it possible to study soliton decay and soliton collisions. The soliton decay rate was found to be approximately twice the linear rate, as expected from theory. The collision of solitons was found to occur with no significant change in shape and velocity. The various characteristic times from theory for pulse decay, pulse dispersion, nonlinear response, and propagation are found to be consistent with the experimental results.

I. INTRODUCTION

The unique capability of solitons to preserve their shape during propagation and to emerge unchanged after collision makes them promising for many applications. Optical solitons in fibers,[1,2] for example, are currently being utilized in long-distance data transmission.[3–6]

This work is concerned with microwave solitons in magnetic films. The first observation of microwave magnetic envelope (MME) solitons in single-crystal yttrium iron garnet (YIG) films was reported in 1983.[7] In parallel with the development in optics, the study of single and multiple MME solitons in magnetic films is likely to lead to new classes of thin-film high-frequency devices for microwave signal processing. Several different MME soliton configurations have been investigated during the last decade. Bright MME solitons have been observed in YIG films for (a) magnetostatic forward volume wave (MSFVW) pulses in films with pinned[7] as well as unpinned[8–11] surface magnetic spins, (b) magnetostatic surface wave (MSSW) pulses in films with pinned surface spins,[12] and (c) magnetostatic backward volume wave (MSBVW) packets for films with unpinned surface spins.[13,14] In addition, dark MSSW envelope solitons have recently been generated in films with unpinned spins.[15]

The specific configuration considered here is for forward volume wave solitons excited by short input pulses. Because of the wide frequency spectra of these pulses, the surface pinning conditions are not critically important, and even a film with rather big dipole-exchange notches may be considered as "unpinned." The publications of Kalinikos and co-workers[8,9] on solitons of this type have clearly demonstrated the evolution of envelope solitons when the power level of a short 4–45 ns wide input microwave pulse becomes higher than a certain threshold value. This group has also reported decay rates for MSFVW solitons which are twice the decay rate for linear pulses,[16] a result expected from theoretical considerations. These experiments, however, did not always involve pure MSFVW signals. An angle was introduced between the static magnetic field and the film normal in order to adjust the conditions of soliton excitation at fixed field magnitude to a single frequency.

De Gasperis and co-workers[10,11] have also reported on MSFVW solitons in YIG films. These workers used 9–107 μm thick films and measured the dependence of the output pulse peak power on input pulse power. Pulse profiles were not monitored. A nonlinear increase in the output peak power above some threshold was observed. This threshold was found to scale with the inverse of the square of the input pulse width, as expected from soliton theory. The nonlinear increase in peak power above threshold was attributed to a decrease of the propagation loss due to soliton formation. Such an explanation is inconsistent with the decay rate results cited above. The nonlinear increase in pulse peak power and decay has been discussed in the context of backward volume wave soliton measurements in Ref. 14.

This work addresses the general problem of MSFVW solitons in YIG films with unpinned surface spins and the issues pointed out above. The experiments included both pulse-shape monitoring and peak power measurements. No angle was introduced between the film normal and the static magnetic field, so that pure MSFVW signals were realized. The basic results of the previous publications are confirmed by these new measurements. In addition, several new aspects of MSFVW soliton phenomena are examined: broadband operation, reflection of soliton pulses from film edges, and soliton attenuation and collision.

The experiments were carried out at fixed field and over the low wave-number end of the MSFVW frequency band in a range 5.6–6.0 GHz. Pulse powers up to 3 W and rectangular microwave pulses with 5–50 ns pulse widths were used. The characteristic increase in pulse amplitude and nar-

[a]On leave of absence from Institute of Electronics, Bulgarian Academy of Sciences, Sofia, Bulgaria.

 0021-8979/94/76(7)/4274/16/$6.00 © 1994 American Institute of Physics

rowing in pulse width associated with soliton formation was observed above threshold, as well as a saturation in the output peak power and the formation of multiple pulse profiles at higher powers. The formation of MSFVW solitons is not critical with respect to frequency within the band of allowed modes. Soliton decay rates were determined from measurements of peak power amplitude as a function of propagation time for pulses reflected from the film edge. In the region of single soliton formation, the decay rates were very close to twice the decay rates for linear pulses, in agreement with Ref. 16. The reflection of pulses from the film edge was also used to produce and observe soliton collisions. Collisions resulted in practically no change of shape and velocity for the interacting solitons. In the discussions of all experimental results, comparisons were made with various predictions from theory based on the so-called nonlinear Schrödinger equation[1,4,17–21] and various characteristic times[21] relevant to linear and nonlinear MME pulse propagation and soliton formation.

Section II summarizes basic theoretical considerations for linear and nonlinear MSFVW MME pulse propagation and establishes the four characteristic times which define the processes of soliton formation and observation. Section III describes the film properties, the microwave transducer structure for the generation and detection of MME pulses, the measurement setup, and the procedures used for the measurements. Results on the propagation characteristics of MSFVW pulses in the linear low power regime are also presented in Sec. III. Section IV presents the measurement results on the propagation, evolution, decay, and collision of the MSFVW MME solitons. The general approach here, as well as the specific notation used below, is the same as in a recent paper[14] by the same authors on backward volume wave MME solitons. Reference 14 will be cited frequently throughout this paper. It contains a comprehensive review of backward volume wave, surface wave, and forward volume wave MME excitations in YIG films, a detailed discussion of MME soliton formation, and a complete bibliography.

II. FORWARD VOLUME WAVE MME PULSES AND SOLITONS

This section summarizes basic equations and parameter definitions for MME wave-packet propagation in thin films, conditions for soliton formation from such packets, and the four characteristic times which are important for soliton formation and detection. Figure 1 shows the narrow, end tapered YIG film, the microwave transducer structure used to generate and detect the MME pulses, and the x-y-z geometry for the analytic description of the magnetic response. The YIG film and transducer structure will be considered in more detail in Sec. III. Note that the y direction is into the page. The YIG film is in the x-y plane and a static external field $\mathbf{H}_{ext}$ is applied parallel to the z axis and perpendicular to the film plane. The net static internal field $\mathbf{H}$ and the static component of the magnetization vector $\mathbf{M}$ will also be perpendicular to the film plane. This configuration is known to support propagating magnetostatic forward volume waves in the film.[22,23] Due to the rotational symmetry with respect to the z axis, any direction can be chosen for the wave vector $\mathbf{k}$.

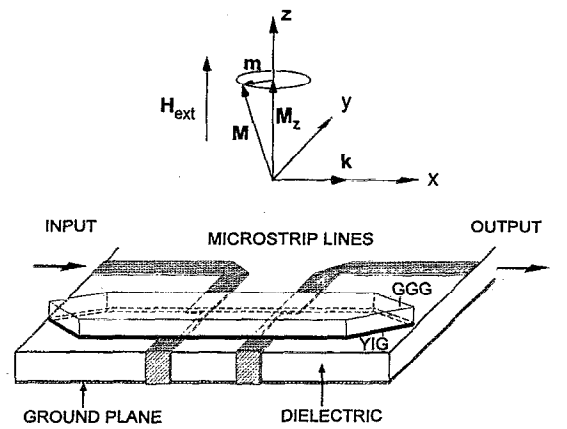

FIG. 1. Diagrams of the magnetization-field geometry for the yttrium iron garnet (YIG) film and the YIG film transducer structure for the experiments. The static internal field $\mathbf{H}$ is along the z direction, perpendicular to the film plane. The magnetization vector $\mathbf{M}$ precesses about this field with a static component $\mathbf{M}_z$ and a dynamic magnetization $\mathbf{m}$ in the x-y and film plane. The magnetostatic wave vector $\mathbf{k}$ is along to the positive x direction. The structure consists of two planar microstrip transmission lines which narrow down to input and output transducer sections. The long and narrow YIG film on a gadolinium gallium garnet substrate is positioned YIG side down over the transducer sections of the input and output microstrip lines. The narrow ends of the YIG film are tapered.

In the present case, the use of a long and narrow rectangular YIG film and microstrip transducer lines across the film as shown gives propagation for a narrow range of angles about the x direction. Therefore, $\mathbf{k}$ can be assumed parallel to the long dimension of the film.

As indicated in the upper diagram, the magnetization response at any point in the sample involves a generally elliptical precession of the total vector magnetization $\mathbf{M}$. The ellipticity is caused by the nonzero divergence of the dynamic magnetization in the direction of propagation. The precession is nearly circular for a small magnitude of the wave vector $\mathbf{k}$. It is also assumed that the magnitude of $\mathbf{M}$ at any point in the film is equal to the saturation magnetization M_s for the material.

Under the above conditions, the MME wave packet may be described by a complex envelope wave-packet response function $u(x,t)$ defined by

$$m_x(x,t)=M_s u(x,t)e^{-i(kx-\omega_k t)} \tag{1}$$

and

$$m_y(x,t)=-iM_s u(x,t)e^{-i(kx-\omega_k t)}, \tag{2}$$

where $m_x(x,t)$ and $m_y(x,t)$ are the x and y components of the dynamic magnetization associated with the packet, ω_k the MSFVW carrier signal frequency, and k the wave number at frequency ω_k. Only the variation of the dynamic magnetization along the propagation direction is considered. The y and z dependencies of the dynamic magnetization are neglected due to the small dimensions of the film along the sample width and thickness.

Magnetostatic waves (MSW) in YIG films magnetized perpendicular to the film plane were first studied by Damon and van de Vaart.[22] The properties of MSFVW wave packets of low amplitude are usually defined in terms of the disper-

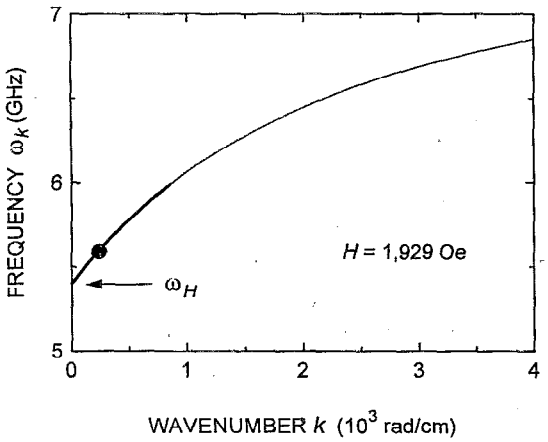

FIG. 2. Calculated dispersion curve of frequency ω_k vs wave number k for magnetostatic forward volume waves (MSFVW). The curve is for a 7.2 μm thick yttrium iron garnet film with a static internal magnetic field of 1929 Oe perpendicular to the film plane. The MSFVW lower limit frequency ω_H at 5.4 GHz, the main operating point at 5.6 GHz, and the useful 5.4–6.0 GHz low transmission loss MSFVW frequency range are indicated by the arrow, solid circle, and heavy line, respectively.

sion curve of ω_k vs k for such waves. A representative MSFVW dispersion curve is shown in Fig. 2. The curve is calculated from the theory of Ref. 24 for a normally magnetized thin YIG film and a net static internal field H of 1929 Oe. The film is taken to have a saturation induction $4\pi M_s$ of 1750 G. The gyromagnetic ratio for the net electron magnetic moments in the YIG material is taken to have an absolute value γ which is the same as for free electrons, 2.8 GHz/kOe.

The dispersion curve in Fig. 2 has a minimum frequency point of 5.4 GHz at $k=0$, for the particular choice of $H=1929$ Oe. This point is labeled as ω_H. This frequency marks the bottom of the MSFVW band. The filled circle at $\omega_k=5.6$ GHz indicates one particular operating frequency which will be used for most of the measurements. The portion of the curve between 5.4 and 6.0 GHz is shown by a heavy line. This is the range of frequencies over which the transmission loss for MSFVW signals is small enough to allow propagation of MME pulses and detection of these pulses at the output transducer. These points will be considered in more detail in Sec. III.

The slope of the dispersion curve in Fig. 2 is positive for all values of k. This corresponds to positive values for the slope parameter $v_g=\partial\omega_k/\partial k$ as well. This v_g is the conventional group velocity for a relatively wide wave packet. A positive v_g is the basis for the "forward volume wave" label for this class of MSW signals. The curvature of the dispersion curve is nonzero and negative. It will prove convenient to define a dispersion coefficient as the value of $\omega_k''=\partial^2\omega_k/\partial k^2$ at the chosen operating point. It is clear from Fig. 2 that the dispersion coefficient for MSFVW wave packets is always negative. Both v_g and ω_k'' will be important parameters for MSFVW solitons. For the parameters given above and the 5.6 GHz operating point in Fig. 2, the theory gives $v_g=4.76\times10^6$ cm/s and $\omega_k''=-2.9\times10^3$ cm^2/rad s. As discussed in Sec. III, it is also possible to determine v_g and ω_k'' empirically from propagation time measurements. The experimental value for v_g under the conditions described above and at $\omega_k=5.6$ GHz is 4.57×10^6 cm/s. The experimental value of ω_k'' is -2.25×10^3 cm^2/rad s. These empirical values will be used for the various estimates and parameters calculated below. Note that "rad" is included in the units specification for ω_k'' given above. This convention will be followed for all parameters involving frequency or wave number, as appropriate, to avoid confusion over the 2π factors involved in the frequency conversion between Hz and rad/s.

The wave-packet carrier frequency ω_k for low level MSFVW excitations must be within a certain frequency band. The lower frequency limit for this band corresponds to the 5.4 GHz intersection point of the ω_k vs k curve with the ω_k axis at $k=0$ in Fig. 2, already identified as ω_H. In general, for a given value of H, this lower frequency limit is given by

$$\omega_H=\gamma H. \tag{3}$$

With $\gamma=2.8$ GHz/kOe and $H=1929$ Oe, one obtains $\omega_H=5.4$ GHz. The upper MSFVW frequency limit is given by

$$\omega_B=\gamma[H(H+4\pi M_z)]^{1/2}. \tag{4}$$

For the specific YIG parameters and H value given above, and under conditions of low level excitations so that $M_z\approx M_s$ is satisfied, ω_B is approximately 7.5 GHz and somewhat higher than the range of frequencies shown in Fig. 2. The ω_H and ω_B limits given above are the same as the limiting frequencies for the low amplitude spin-wave band at $k=0$. It is important to note that the operating point in Fig. 2 is relatively close to ω_H.

Turn now to the effects of increasing power on the MSFVW excitations described above. The key effect is contained in the change in M_z relative to M_s as $m_x(x,t)$ and $m_y(x,t)$, and hence, $u(x,t)$, become larger. From the above equations and the condition $|\mathbf{M}|=M_s$, one can obtain an immediate connection between M_z and M_s. To lowest order in $|m_x|$ and $|m_y|$, this connection is given by

$$M_z=M_s-\frac{|m_x(x,t)|^2+|m_y(x,t)|^2}{2M_s}=M_s(1-|u(x,t)|^2). \tag{5}$$

It is important to note that the static internal field H is also a function of M_z. For the film-field geometry shown in Fig. 1, H may be written as

$$H=H_{\text{ext}}+H_A-4\pi M_z, \tag{6}$$

where the H_A term represents an effective anisotropy field and the $-4\pi M_z$ term accounts for the demagnetizing field for the perpendicular-to-plane magnetized thin film. For the relatively high power levels which will be important for solitons, the values of $|m_x|$ and $|m_y|$ will be big enough to have a significant influence on the z component of the magnetization and, therefore, on ω_H and ω_B as well. The quantity $|u(x,t)|^2$ will turn out to be am important parameter in the nonlinear-response analysis. For convenience, $|u(x,t)|^2$ will be termed *power amplitude*.[14]

The usual approach to model the spatial and temporal evolution of the $u(x,t)$ in low-loss, dispersive magnetic films at high power levels involves use of the so-called nonlinear Schrödinger equation.[1,4,14,17–21] This equation will be used here as a basis for the introduction of various parameters which are important to the understanding of nonlinear MME pulse propagation in YIG films. The appropriate form of the equation for a long and narrow magnetic film with propagation only in the x direction is

$$i\left(\frac{\partial u}{\partial t}+v_g\frac{\partial u}{\partial x}+\eta u\right)+\frac{1}{2}\omega_k''\frac{\partial^2 u}{\partial x^2}-N|u|^2u=0. \tag{7}$$

The left side of Eq. (7) contains three terms. The first term describes damped propagation, the second term adds the effect of dispersion, and the third term brings in the nonlinearity. In the first term, v_g is the group velocity for a relatively wide wave packet as already defined. The η parameter denotes the low power relaxation rate for the dynamic magnetization $\mathbf{m}(x,t)$, and the response function $u(x,t)$ as well, associated with the propagating MSW signal. This relaxation rate is a critical parameter in the decay of both linear and nonlinear MME wave packets. The ω_k'' factor in the second term, the dispersion coefficient already discussed in connection with Fig. 2, relates to the curvature of the ω_k vs k dispersion relation for low amplitude signals. In the absence of other effects, this term leads to the usual dispersion broadening of the wave packet. The N coefficient in the last term on the left-hand side of Eq. (7) is a nonlinear-response parameter defined as the rate of change in the MSW frequency ω_k with respect to the power amplitude $|u(x,t)|^2$ and evaluated at $|u(x,t)|=0$:

$$N=\frac{\partial\omega_k}{\partial|u|^2}. \tag{8}$$

The relative signs of the dispersion coefficient and the N coefficient are critical to soliton formation. The basic effect is due to competing frequency shifts. When the frequency shift due to dispersion, which is proportional to ω_k'', and the frequency shift due to the nonlinear response, which is proportional to N, have opposite signs, one has the possibility of compensation between the frequency shift due to dispersion and the nonlinear frequency shift. This leads to pulse narrowing and soliton formation. This sign condition may be expressed as[1,14,17,25]

$$\omega_k''N<0. \tag{9}$$

This condition is sometimes termed the "Lighthill" criterion.[9,12]

The N parameter may be estimated from the formal response equations given above, under the assumptions that (1) the carrier frequency ω_k is close to ω_H, (2) the effect of $|u|^2$ on ω_k occurs predominantly through the change in M_z, and (3) the small change in the anisotropy field H_A with $|u|^2$ has little effect on ω_k. The result is

$$N=\gamma 4\pi M_s=\omega_M. \tag{10}$$

The ω_M parameter in Eq. (10) simply expresses the saturation induction $4\pi M_s$ in frequency units. For $4\pi M_s=1750$ G, one has $N=\omega_M=4.9$ GHz$=3.08\times10^{10}$ rad/s. The size of the N coefficient is noteworthy. A value of 10×10^{-4} for $|u|^2$, corresponding to a $|\mathbf{m}|/M_s$ ratio of about 3%, leads to a 5 MHz frequency shift in ω_k. The $|u|^2$ values encountered in the soliton experiments will be on the order of $|u|^2=1-10\times10^{-4}$.

Under conditions for which the Lighthill criterion is satisfied, one may obtain analytical pulse solutions to Eq. (7).[26,27] In the MSFVW case of interest here for YIG films with unpinned surface spins and for small damping, the single pulse solution may be written in simplified form as

$$|u(x,t)|=u_0e^{-2\eta t}\,\mathrm{sech}\left[u_0e^{-2\eta t}\sqrt{\left|\frac{N}{\omega_k''}\right|}(x-v_gt)\right]. \tag{11}$$

In this expression, the difference between the soliton velocity and the linear group velocity v_g has been neglected.[8]

The hyperbolic secant pulse shape described by Eq. (11) embodies several basic soliton characteristics which will be important in the experiments. First, note that the initial amplitude at $t=0$, u_0, and the corresponding temporal width T_0 of the $|u(x,t)|$ pulse at $x=0$ are related

$$T_0^2|u_0|^2=\frac{1}{v_g^2}\left|\frac{\omega_k''}{N}\right|. \tag{12}$$

This connection demonstrates the nonlinear eigenmode characteristic for solitons. According to Eq. (12), one may produce a single soliton only for a specific relationship between pulse amplitude and width. If one goes to either lower amplitudes or narrower pulses, one no longer has the proper conditions to produce the soliton pulse and one sees only the usual dispersion broadening expected in the linear regime. If one goes to either higher amplitudes or wider pulses, the proper conditions to produce a single soliton pulse are also not satisfied. In this case, one observes multiple soliton pulses. These effects were demonstrated experimentally for MSBVW solitons in Ref. 14. Related pulse power and pulse widths effects for MSFVW solitons will be demonstrated by the experiments presented below.

Second, note the decay characteristics for the pulse described by Eq. (12). The amplitude of the pulse, given by $u_0e^{-2\eta t}$, decays at a rate 2η. The decay rate for low amplitude pulses in the linear regime is simply η. The decay rate for solitons, therefore, is *twice* the rate for linear signals. As already indicated, this factor of 2 increase in decay rate for MSFVW solitons was observed experimentally by Kalinikos and co-workers.[16] In the present work, the effect is confirmed from decay measurements on soliton pulses reflected from the film edges.

Finally, note that the single soliton condition of Eq. (12) is a function of the dispersion parameter ω_k'', the nonlinear-response N parameter, and the group velocity v_g. The soliton condition will be determined by the values of these parameters at the (ω_k,k) operating point of interest. In order to minimize propagation time and propagation loss, one generally chooses an operating point with a relatively large v_g. For MSFVW pulses, this corresponds to an operating point close to ω_H, as in Fig. 2. One of the new results of this MSFVW soliton study is in the generation and detection of

similarly behaved solitons over a frequency range which extends significantly above ω_H, corresponding to the 5.4–6.0 GHz range shown in Fig. 2. This result will be discussed in terms of the frequency dependence of the ω_k'', N, and v_g parameters and the corresponding conditions for soliton production.

The same basic single soliton $T_0^2|u_0|^2$ critical product result discussed above can be obtained from more physical and somewhat less formal arguments based on the various characteristic times for MME pulses.[14] This section is concluded with a brief discussion of these times. Such characteristic times are used extensively for optical solitons.[21] These times will play an important role in the interpretation of the experimental MSFVW soliton results. Four characteristic times are involved, a relaxation time T_r, a dispersion time T_d, a nonlinear-response time T_n, and a propagation time T_p.

The relaxation time T_r is the $1/e$ decay time for $|u(x,t)|$ associated with relaxation at low amplitude

$$T_r = 1/\eta. \tag{13}$$

As discussed in Secs. III and IV, low power pulse decay measurements can be used to determine the relaxation rate η and, hence, T_r. The present measurements give $\eta = 5.2\times10^6$ rad/s and $T_r = 190$ ns.

A dispersion time T_d may be defined as the time for a pulse of width T_0 to double in width because of dispersion. If the frequency spread for the pulse is taken as $1/T_0$ and the change in group velocity over this spread is then estimated at $\omega_k''/v_g T_0$, one obtains

$$T_d = \frac{v_g^2 T_0^2}{|\omega_k''|}. \tag{14}$$

Based on the values of v_g and ω_k'' cited above, one obtains $T_d(\text{ns}) = 9.3[T_0(\text{ns})]^2$. Note that an initial pulse width below $T_0 = 5$ ns is needed for the dispersion time T_d to fall below the relaxation time $T_r = 190$ ns given above.

In a similar manner, a nonlinear-response time T_n may be defined as the time required for the phase of the MME pulse carrier signal to change in phase by π radians when the power amplitude is increased from some very low value to some $|u_0|^2$. This characteristic time is

$$T_n = \frac{\pi}{|N||u_0|^2}. \tag{15}$$

For the numerical value of N given above, one obtains $T_n(\text{ns}) = 1020/[|u_0|^2\times10^4]$. In order for the nonlinear-response time to fall below the relaxation time given above, $|u_0|^2$ must be greater than 5×10^{-4}. This corresponds to a dynamic magnetization amplitude on the order of a few percent of the saturation magnetization M_s. It is clear, therefore, that nonlinear effects are possible for relatively low amplitude MME signals.

The propagation time T_p is simply the time required for the pulse to travel between the input and output transducers in the experimental setup. For the arrangement in Fig. 1, with a transducer spacing L, T_p is given by

$$T_p = L/|v_g|. \tag{16}$$

For the transducer spacing of 0.4 cm for the present experiment, the measured propagation time for MSFVW pulses at 5.6 GHz and under conditions shown in Fig. 1 is 87.6 ns. This time was the basis for the empirical v_g value cited above. Note that this propagation time is about a factor of 2 smaller than the relaxation time given above. In addition, this T_p is in the same range as the dispersion and nonlinear-response times obtained above for pulse widths in the 5 ns range and power amplitudes in the $|u_0|^2 \approx 5\times10^{-4}$ range. It is clear, therefore, that nonlinear MME pulses observed experimentally must be interpreted with care. All the characteristic times are comparable in size.

As indicated at the beginning of this characteristic time discussion, these times also lead to a $T_0^2|u_0|^2$ critical product for solitons. This result is obtained from the realization that the nonlinear phase change can compensate for the dispersion spreading only if the nonlinear response time T_n is *smaller* than the dispersion time T_d. As in Ref. 14 the condition $T_n < T_d$ can be used to obtain a minimum value of the $T_0^2|u_0|^2$ product for soliton formation. The condition $T_n = T_d$ gives $T_0^2|u_0|^2 = (\pi/v_g^2)|\omega_k''/N|$, which is the same as Eq. (12) except for a factor of π. A formal analysis which explicitly takes the possibility of exciting more than one soliton[20] gives a more general critical product expression,

$$T_0^2|u_0|^2 > (n-\tfrac{1}{2})^2 \frac{\pi^2}{|v_g|^2}\left|\frac{\omega_k''}{N}\right|, \tag{17}$$

where n is an integer which denotes the number of solitons. Equation (17) has the same basic form as Eq. (12), but with an additional $(n-1/2)^2\pi^2$ factor. Based on the numerical values for the various parameters given above, Eq. (17) may be cast in more practical form as

$$[T_0(\text{ns})]^2[|u_0|^2\times10^4] > 86(2n-1)^2. \tag{18}$$

Equation (18) demonstrates the scale of pulse widths and power amplitudes which are needed to produce solitons. The single soliton $n=1$ critical product $[T_0^2|u_0|^2\times10^4] = 86$ ns^2, for example, gives $|u_0|^2 \approx 10^{-4}$ at $T_0 = 10$ ns. From the other conditions given above, one also has $T_d = 930$ ns and $T_n = 1020$ ns. These later two times are significantly greater than the relaxation time of 190 ns or the propagation time of 90 ns. This means that whatever nonlinear solitonlike pulses are observed experimentally, the measured single soliton signals under critical product conditions correspond to solitons which are only in the initial stages of formation.

From Eq. (18), the critical product increases rapidly as the soliton number index n is increased. Values of the $[T_0^2|u_0|^2\times10^4]$ critical products for two, three, and four solitons are 780, 2160, and 4240 ns^2, respectively. The multiple soliton situation will depend on whether one satisfies the higher critical product requirement by increasing the power, and hence $|u_0|^2$, or by increasing the pulse width. As $|u_0|^2$ increases, the nonlinear response time T_n will decrease. Since T_n corresponds more or less to the soliton formation time, one will be observing a soliton farther and farther along in its formation process. If, on the other hand, one increases T_0 to increase the $T_0^2|u_0|^2$ product, this serves only to increase the dispersion time while leaving T_n and the soliton formation time unchanged.

From the perspective of soliton formation time relative to the propagation time, it is useful to define one final critical parameter, a critical power amplitude $|u_0|^2_{pn}$ at which T_n will fall below T_p. For the numerical values listed above, this condition yields $|u_0|^2_{pn} \times 10^4 = 11.6$. This means that under the MSFVW conditions established above, a power amplitude $|u_0|^2$ on the order of 10×10^{-4} or greater, corresponding to a dynamic magnetization on the order of 3% of M_s or greater, will guarantee that the soliton formation time is smaller than the propagation time. Under these conditions, one would expect to see more-or-less completely formed solitons in the experiment. This limit on $|u_0|^2$ translates into critical pulse widths of 3, 8, 14, and 19 ns for one, two, three, and four soliton signals.

It is important to realize that none of the above limits represent hard conditions on either the creation or the observation of soliton behavior. The various characteristic times are defined somewhat arbitrarily, in terms of a $1/e$ decay for T_r, a doubling in pulse width for T_d, and a phase change of π for T_n. Other definitions could have been used as well. The critical product from Eq. (18), for example, represents more a rule of thumb than a definite threshold for n solitons. The propagation time constraint, moreover, simply means that whatever behavior is observed may correspond to incomplete soliton formation if T_n is well above T_p.

In concluding this section, consider finally the conditions to avoid first-order spin-wave instability effects.[28] The main requirement here is that there be no available spin-wave states at one-half the excitation frequency. In the present situation, shown in Fig. 2, the bottom of the MSFVW dispersion curve and the bottom of the spin-wave band are at 5.4 GHz. The highest frequency at which soliton signals were observed in the experiments was 6 GHz. The 3 GHz half-frequency point for such signals is well below the bottom of the band. First-order spin-wave instability effects are not important here.

III. EXPERIMENT AND LOW POWER MSFVW PROPAGATION MEASUREMENTS

This section describes the experimental arrangement for the excitation of MSFVW wave packets in YIG films and the low power characterization of MSFVW signals. The experiments were performed at room temperature and utilized a YIG film microstrip magnetostatic wave transducer line structure[14] in the forward volume wave configuration as shown in Fig. 1. Section III A describes the experimental setup. Section III B gives results on the linear MSFVW wave-packet propagation characteristics for the structure. As for the MSBVW measurements in Ref. 14, these results provide a check on the nature of the magnetostatic wave signals under study and yield an empirical determination of two key MSW parameters introduced in Sec. II, v_g and ω''_k. Section III C gives a summary of the basic parameters and operational relations important for the MSFVW soliton measurements and analysis.

A. Experiment

The YIG films used in this work were provided by Dr. J. D. Adam, Westinghouse Research and Development Center, Pittsburgh, Pennsylvania. They were grown on (111) plane single-crystal gadolinium gallium garnet substrates by the method of liquid-phase epitaxy (LPE).[23] Film thicknesses were estimated from the LPE processing parameters. The results presented below are for samples cut from one particular LPE sample with a 7.2 μm thick YIG film. Similar results were found for other films of comparable thicknesses. The films were characterized by a ferromagnetic-resonance (FMR) technique at 9.5 GHz for both in-plane and perpendicular-to-plane static fields and different size rectangular samples. These FMR spectra, while complicated, were consistent with the magnetic parameters given above, a film in the (111) crystallographic plane film, and a small contribution to the net static internal magnetic field H due to the cubic magnetocrystalline anisotropy. From the low power cw MSFVW measurements on the actual transducer structure, discussed below, this anisotropy field was set at -65 Oe. The peak-to-peak derivative linewidths for the low-order magnetostatic modes in the in-plane field FMR configuration at 9.5 GHz were about 0.35 Oe.

The MSW transducer structure shown in Fig. 1 was used in the experiments. Standard input and output 50 Ω microstrip transmission line sections connect to transducer line sections under the YIG film which are 2.5 mm long and 50 μm wide. These lines are on the top surface of a RT/Duroid® laminate dielectric substrate with a conducting ground plane backing. The separation between the input and output transducer lines is 4 mm. Most of the measurements were carried out on one 2 mm×15 mm YIG film sample. As shown schematically in Fig. 1, the ends of the 2 mm×15 mm strip were tapered in order to reduce unwanted reflections. The sample was positioned with the center section of the strip over the transducers as indicated in Fig. 1. The MSW signals were propagated parallel to the long direction of the sample from one transducer to the other. As already discussed in Sec. II, the assembly was placed in a static external magnetic field perpendicular to the plane of the film. This configuration corresponds to the forward volume wave configuration described in detail in Sec. II. Some experiments used a different 2 mm×12.5 mm YIG strip with carefully prepared rectangular ends rather than tapered ends, and with the film shifted to position the output transducer closer to one end of the strip. In such a configuration, MSW pulses could be detected by the output transducer before and after reflection from the end of the strip.

The microwave measurements utilized the same equipment described in Ref. 14. Figure 3 shows the block diagram of the overall setup. The key elements are the HP83640A synthesized microwave source, the fast GaAs microwave switch, and the HP71500A microwave transition analyzer. The fast switch allows for the production of microwave pulses with widths down to 2–3 ns and rise times below 1 ns. The HP71500A analyzer can be operated both as a network analyzer and as a fast digital sampling oscilloscope. This dual mode of operation is useful for the *in situ* study of the transducer structure, MSFVW transmission loss and passband properties, and MSFVW pulse propagation.

For measurements in the time domain, the synthesized source provides the cw carrier signal, while the pulse gen-

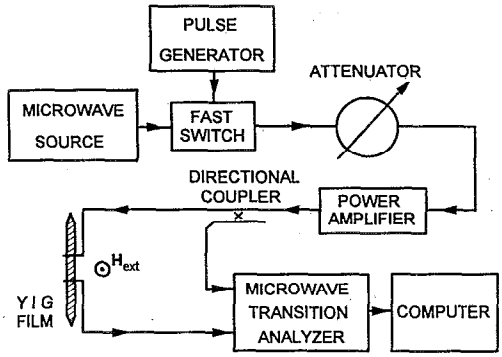

FIG. 3. Block diagram of the microwave measurement system.

erator and the switch provide for the generation of pulses. Typical operation utilized a 1 kHz repetition rate and pulse widths up to 100 ns, for a duty cycle below 0.01%. Such low duty cycles were adequate to avoid heating effects. For frequency domain measurements, the synthesizer provides a variable frequency cw microwave signal source with the microwave switch maintained in the "on" mode.

B. Linear MSFVW propagation parameters

Figure 4 shows an experimental transmission loss versus frequency curve for the MSFVW signal through the transducer structure measured at power level of about 1 mW and with an external static magnetic field of 3744 Oe. This field value was selected to position the low-frequency cutoff point at the ω_H frequency point of 5.4 GHz. This cutoff is indicated by the vertical arrow in Fig. 4 and the "ω_H" label. The transmission passband from this cutoff up to about 6 GHz is evident in the figure. Above 6 GHz or so, the decrease in coupling efficiency from the microstrip transducer to high wave-number spin MSW signals and the lower group velocity for the propagating MSFVW excitations push the detected signal below the background signal for the structure.

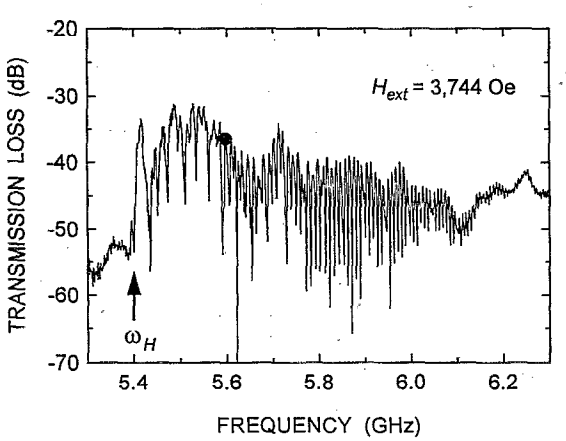

FIG. 4. Measured transmission loss vs frequency at low power for the YIG film transducer structure of Fig. 1 in the MSFVW configuration. The film thickness was 7.2 μm and the external applied field was 3744 Oe. The input cw microwave power was about 1 mW. The arrow marks the lower edge of the MSFVW frequency passband at $\omega_H = 5.4$ GHz. The solid circle on the loss curve at 5.6 GHz marks the main operating point for the experiments.

The solid point at 5.6 GHz indicates the operating point already discussed. This point is positioned 200 MHz above the bottom of the passband.

The shape of the transmission loss profile for the MSFVW signals in Fig. 4 is not as simple as one would expect from the dispersion curve in Fig. 2. The profile shows two complicating features. The first complication is in the spurious ripple which is superimposed on the transmission curve. This ripple is due to interference of the MSW signal with microwave leakage through the structure. The second complication concerns the pronounced notches evident in Fig. 4. These notches are due to dipole-exchange gap effects. These gaps occur where the main MSFVW dispersion branch shown in Fig. 2 crosses the various higher-order exchange branches of the dispersion.[24] If there was no pinning, these gaps would be so narrow that they would be unresolved on the scale of Fig. 4. Surface spin pinning widens the gaps and leads to notches in the transmission loss profile.[23,29,30] The notches in Fig. 4, while distinct, are smaller than the notches for films with pronounced surface spin pinning.[30] The experiments described below involve short, 5–50 ns wide pulses. The 20–200 MHz frequency broadening for such pulses, to be discussed in more detail below, is much bigger than the narrow dipole-exchange gaps in Fig. 4. The moderate pinning apparent in Fig. 4, therefore, has no practical effect on any of the results considered below.

In connection with the above remarks on pinning, it is pertinent to note that these same films were used for the work on backward volume wave solitons and dark surface wave solitons reported previously.[14,15] The films were taken to be unpinned in both cases. In the backward volume wave case, the presence of pinning does not produce dipole-exchange gaps and would have little effect on the solitons. In the surface wave case, the measured transmission loss curves showed very small notches, even smaller than in Fig. 4. Here, too, pinning effects are negligible.

As already noted, the value of the static external magnetic field required to position the ω_H band edge for the data in Fig. 4 at 5.4 GHz is 3744 Oe. From Eq. (3), and with the γ value of 2.8 GHz/kOe already cited, 5.4 GHz corresponds to a net static internal field $H = 1929$ Oe. Equation (6) with these H and H_{ext} values, and with $4\pi M_s = 1750$ G, gives an effective anisotropy field $H_A = -65$ Oe. This negative H_A value is consistent with FMR measurements on these same films with the static magnetic field perpendicular to the film plane. If H_A is due only to magnetocrystalline anisotropy, one would expect H_A values for [111] magnetized YIG in the range +80 to +90 Oe. It appears that the full anisotropy includes other effects such as stress and growth-induced anisotropies.

The characteristic MSFVW dispersion curve of frequency $\omega_k(k)$ versus wave number k which corresponds to the transmission loss profile of Fig. 4 was shown in Fig. 2 and discussed in Sec. II. Comparison of the frequency scales for Figs. 2 and 4 shows that the observable passband upper limit in frequency of 6 GHz or so corresponds to wave numbers of about 10^3 rad/cm. The corresponding wavelength is about the same as the 50 μm transducer width. MSW signals at higher wave numbers and shorter wavelengths are not

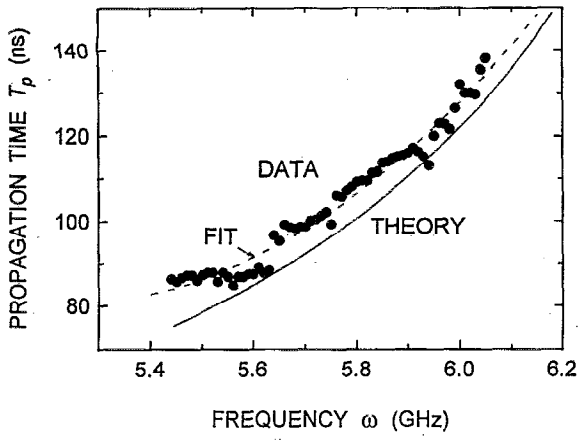

FIG. 5. Propagation time T_p vs frequency ω for the YIG film transducer structure and low power MSFVW pulses. The film thickness was 7.2 μm and the external applied field was 3744 Oe. The microwave input pulses were 150 ns wide and the input pulse peak power was 1.5 mW. The input and output transducer spacing was 4 mm. The solid circles show the data. The solid curve shows the calculated propagation time vs frequency based on the MSFVW dispersion characteristic in Fig. 2. The dashed line shows a smooth curve fitted to the data.

strongly excited. The operation frequency for most of the experiments was chosen at 5.6 GHz, as indicated by the solid dot in Fig. 4. This operating point was selected to be close to the low-frequency edge of the passband, where the attenuation is lowest, and still be far enough from this edge to keep the spectral content of the signal for narrow pulses above the ω_H cutoff. An operating point 200 MHz above the band edge at $\omega_H = 5.4$ GHz makes it possible to use pulse widths as low as 5 ns and still keep most of the microwave spectral content of the pulse within the passband.

In addition to measurements of the transmission loss versus frequency profile, the propagation time between input and output versus frequency was measured for low power MSFVW pulses under the same field conditions as in Fig. 4. From the propagation time at any given frequency, one can determine the group velocity v_g. From the change in propagation time with frequency, one can determine the dispersion coefficient ω_k''. Figure 5 shows representative measurements of the MSFVW pulse propagation time T_p versus frequency ω for the transducer structure already discussed, the same perpendicular-to-film magnetic field as before, 150 ns wide MSW pulses, and a pulse peak power level of 1.5 mW. The measurements are indicated by the solid circles. The solid curve represents the calculated propagation time based on group velocities calculated from the slope of the theoretical MSFVW dispersion curve as a function of frequency. The dashed curve represents a smoothed curve fit to the data.

The data in Fig. 5 show some residual structure due to the notches in the propagation loss versus frequency profiles already discussed. This structure is somewhat washed out because of the pulse nature of the measurement. For the 150 ns pulse used for the propagation time measurements, the microwave spectral width is about 15 MHz. This means that the v_g values in Fig. 5 represent average values over this spread in frequencies. This averaging tends to wash out the exchange gap effects evident from the sharp notches in the cw loss profile of Fig. 4. The solid line shows that the v_g vs ω result derived from the basic MSFVW dispersion curve with no gap effects gives propagation times which are in reasonable agreement with the measurements. The group velocity v_g at the 5.6 GHz operating point, as obtained from the measured propagation time of 87.6 ns and the transducer spacing of 4 mm, is 4.57×10^6 cm/s.

Turn now to the dispersion parameter ω_k''. The dispersion scales with the T_p vs ω response according to $\omega_k'' = -(L^2/T_p^3)(dT_p/d\omega)$. In order to determine the $(dT_p/d\omega)$ slope parameter from Fig. 5 which is appropriate to soliton experiments at any given operating point, it is important to keep in mind the averaging effects due to the finite pulse width already discussed. In the case of the 150 ns pulses used for the T_p vs ω measurements in Fig. 5, the averaging is sufficient to wash out most but not all of the exchange gap effects. For the pulse widths in the 5–50 ns range which are used for the soliton experiments, the spectral width averaging effects will be even more significant. For this reason, the smoothed curve fit to the data shown by the dashed line in Fig. 5 will be used to determine $(dT_p/d\omega)$. This empirical slope, in practical units, is 60 ns/GHz, compared to the theoretical slope of 68 ns/GHz. The empirical slope at the 5.6 GHz operating point, along with the measured value of T_p, gives $\omega_k'' = -2.25 \times 10^3$ cm^2/rad s. The theoretical value from the solid curve in Fig. 5 is -2.9×10^3 cm^2/rad s.

It is clear from the above that ω_k'' cannot, in the present situation, be determined with much precision. It has already been pointed out in Sec. II, in connection with the discussion of characteristic times, critical products, and soliton thresholds, that none of the analytical or numerical limits represent hard conditions on either the creation or the observation of soliton behavior. Except for $|u_0|^2_{pn}$, those limits all depend on ω_k'' in some fashion. In view of the uncertainty in determining ω_k'', these limits must be viewed with even more caution. They should certainly not be taken as rigorous limits for solitons.

C. Summary of parameters

The various parameters discussed above, as well as the working relations for the characteristic times, critical products, and critical amplitudes, are listed in Table I. Where appropriate, the units for frequency and wave number are taken to include explicitly the 2π factor, with frequency parameters in rad/s and wave numbers in rad/cm. Numerical values of parameters have been rounded to represent nominal values. For the results presented below, initial pulse widths, denoted by T_0, will generally be on the scale of tens of nanoseconds and power amplitudes, denoted by $|u_0|^2$, will generally be in the range $1-10\times10^{-4}$. Table I shows T_0 and other characteristic time values in nanoseconds and $|u_0|^2$ values in units of 10^{-4}.

IV. EXPERIMENTAL RESULTS

As with the MSBVW solitons considered in Ref. 14, several different experiments were carried out to investigate

TABLE I. List of parameters.

Parameter	Value
Film thickness	7.2 μm
Transducer separation L	4 mm
Saturation induction $4\pi M_s$	1750 G
Gyromagnetic ratio γ	2.8 GHz/kOe, 1.76×10^7 rad/s Oe
Net internal static field H	1929 Oe
Static external field H_{ext}	3744 Oe
Effective anisotropy field H_A	−65 Oe
Operating frequency ω	5.60 GHz, 3.52×10^{10} rad/s
Frequency limit ω_H	5.40 GHz, 3.39×10^{10} rad/s
Group velocity v_g	4.57×10^6 cm/s
Dispersion coefficient ω_k''	-2.25×10^3 cm^2/rad s
Relaxation rate η	5.2×10^6 rad/s
Nonlinear-response coefficient N	3.08×10^{10} rad/s
Relaxation time T_r	190 ns
Dispersion time T_d	$9.3[T_0(\text{ns})]^2$ (ns)
Nonlinear-response time T_n	$1020/[\lvert u_0\rvert^2\times10^4]$ (ns)
Propagation time T_p	87.6 ns
Critical product $T_0^2\lvert u_0\rvert^2\times10^4$	$86(2n-1)^2$ ns^2
Critical power amplitude $\lvert u_0\rvert^2_{pn}\times10^4$	11.6

MSFVW envelope soliton development. In the basic measurement, the $T_0^2|u_0|^2$ product for the initial input pulse was increased in a systematic way, output pulse profiles were measured, and soliton properties were noted. One set of such measurements was done by keeping the width of the input pulse constant while increasing the input peak power level. For the second set, the input peak power level was held constant while the input pulse width was increased. In both cases, it was possible to observe the formation of sharp and narrow soliton pulses, followed by the successive formation of multiple peak pulses corresponding to multiple solitons. Further measurements were then made of the output pulse peak power versus input pulse power and input pulse width, respectively. The measurements gave thresholds for soliton formation which were consistent with theory.

As indicated in Sec. II, one characteristic of solitons is an increase in the decay rate by a factor of 2 above the linear decay rate. Decay rates were determined for MSFVW pulses in both the low power linear regime and in the soliton regime. These determinations were made, as noted above, from output pulse measurements before and after reflection from the end edge of the YIG film strip. It was also possible to perform these edge reflection experiments with two single soliton pulses and observe, thereby, solitons after passing through each other.

A. Experiments for constant input pulse width

Figure 6 shows a series of input and output power profiles for fixed input pulse width and increasing power. The pulse width was held constant at $T_0=10$ ns. Traces (a)–(d) show profiles for input pulses with average powers of 0.16, 0.9, 2.0, and 2.8 W, respectively. These values were obtained by averaging the input pulse power over the duration of the pulse. The strict values of the peak input powers are slightly higher. Note also that the power scales for the input pulses are in watts, while the power scales for the output pulses are in milliwatts. The input pulse width of 10 ns is not critical in the experiment. It was chosen here to demonstrate the initial

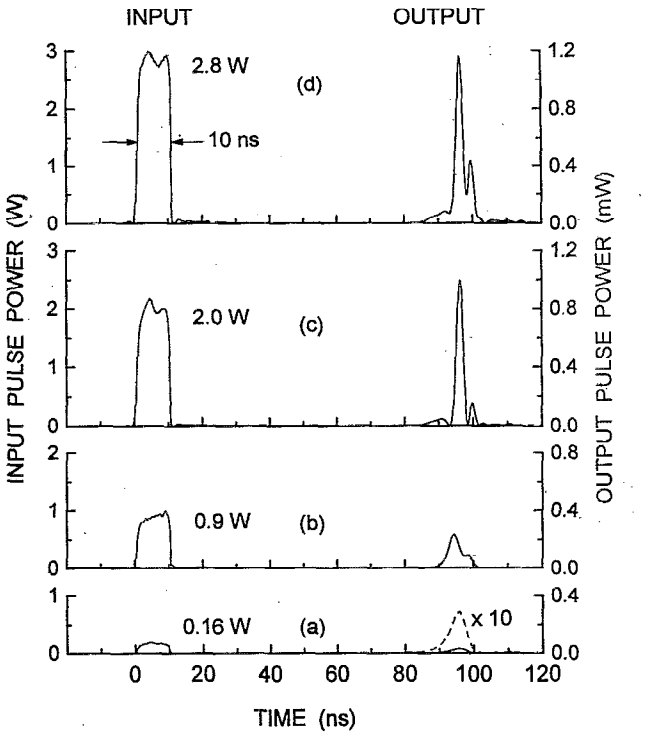

FIG. 6. Input and output profiles of detected power vs time for the YIG film transducer structure of Fig. 1 in the MSFVW configuration for the four different average input power levels indicated. The film thickness was 7.2 μm and the external applied field was 3744 Oe. The carrier frequency was 5.6 GHz and the input pulse width was held constant at 10 ns. The dashed curve for output profile (a) shows the pulse with the vertical response expanded by a factor of 10.

development of a single soliton at a reasonable power level as well as the stages of multiple soliton formation at the highest power levels available in the experiments. With shorter pulses, the single soliton peak does not appear until one reaches power levels near the limit of the present system, while longer pulses tend to produce multiple peaks before the single peak profile is fully developed. Note that the propagation time for all power levels is about 90 ns, the same as for the linear low power regime.

Trace (a) in Fig. 6, for an input average power of 0.16 W, shows no pulse steepening or narrowing. At this low power, the response is in the linear region. The dashed line shows the output profile expanded by a factor of 10 on the power scale. The output pulse has about the same 10 ns width as the input pulse. When the power is increased to 0.9 W, as shown in trace (b), one sees an almost proportional increase in the output pulse height and the same basic shape as in (a). When the input power further increased to 2.0 W, as in trace (c), a steepening and narrowing occurs for the output pulse. This characteristic narrowing and steepening is one indication of soliton formation.[2,7–9,14] The width of the output pulse is now about 2–3 ns, significantly narrower than the input pulse width. The output profile in trace (c) also shows a much smaller second pulse. This may indicate the beginning development of a second soliton peak. The effect of higher power on these two peaks is shown in trace (d), at 2.8 W. Even though there has been a 40% increase in input power,

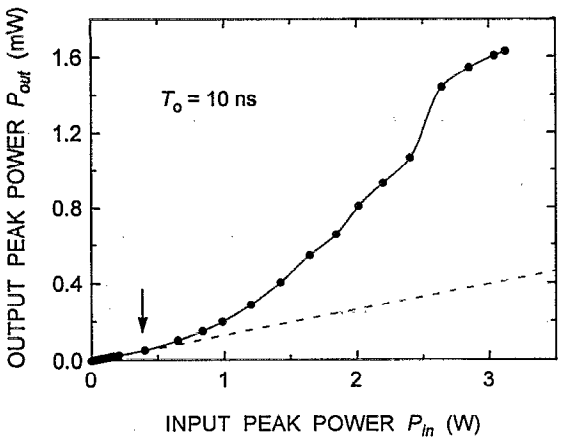

FIG. 7. Measurements of output peak power P_{out} vs input pulse peak power P_{in} for a series of pulse propagation experiments with the YIG film transducer structure of Fig. 1 in the MSFVW configuration and with the input pulse width T_0 held constant at 10 ns. The film thickness was 7.2 μm and the external applied field was 3744 Oe. The carrier frequency was 5.6 GHz. The solid circle data points are connected by a smooth curve. The dashed line indicates the linear dependence extrapolated from the low power response below P_{in}=0.4 W.

the first peak has grown by only 20%. The second, smaller peak, on the other hand, has grown somewhat, relative to the first peak. The fact that the first peak is beginning to stabilize in amplitude indicates that the formation process for the first soliton is nearly complete.

While Fig. 6 shows that one does achieve pulse sharpening and narrowing with increasing power, as well as multiple pulses, these profiles in themselves do not show any clear threshold effect. De Gasperis *et al.*,[10,11] Chen *et al.*,[14] and Nash *et al.*[31] have shown, however, that measurements of output peak power versus input peak power at constant pulse width can yield quantitative determinations for soliton thresholds. Measurements similar to those shown in Fig. 6 were used, therefore, to obtain response curves of output peak power P_{out} versus input peak power P_{in} at constant pulse width. Representative results for the same input pulse length of 10 ns used in Fig. 6 are shown in Fig. 7. The filled circles represent the data. The solid lines connect the data points. The dashed line represents a linear best fit to the data for the lowest input peak power values.

Figure 7 shows that for input peak powers below about 0.4 W the output peak power response is linear. For input peak powers above 0.4 W, the data show a clear departure from this linear response. The break point at P_{in}=0.4 W is indicated by a vertical arrow. Note that this transition from a linear to a nonlinear response occurs at a power which is well below the input peak power level at which the steepening and narrowing effects become obvious from the actual output pulse profiles in Fig. 6. As the input power level moves into the regime where steepening and narrowing occurs for the observed output pulses in Fig. 6, the output peak power continues to increase. There is an inflection point of sorts at P_{in}=2–2.5 W, and the beginnings of an apparent leveling off or peak in the response at powers above 3 W.

The nonlinear increase in the output peak power at a relatively low value of the input peak power is similar to the result found for MSBVW solitons in Ref. 14. The present results also confirm the threshold effect reported in Refs. 10 and 11 for MSFVW pulses. The nonlinear increase in the output peak power above threshold, however, is not due to a reduction in losses, but rather, is due to the pulse steepening and narrowing.[14] However, the data in Fig. 7 do not show a peak in P_{out} vs P_{in} at higher powers as found for MSBVW solitons. Those data showed a significant drop in the output peak power for input peak powers above 2 W or so. In the present MSFVW case, one sees only the beginnings of such a turnaround, if any. Any quantitative interpretation of the data in Fig. 7, however, is complicated. Not only is the $T_0^2|u_0|^2$ product increasing as the peak input power is increased, so that the various soliton thresholds are exceeded one by one. At the same time, the nonlinear response time T_n is decreasing as the peak input power is increased. This decrease means that at the fixed propagation time of 90 ns, one is seeing, as P_{in} increases, the soliton profile later and later in its formation process. This matter of soliton evolution will be considered in more detail shortly.

Following the approach in Ref. 14 for MSBVW solitons, one can associate the initial break at P_{in}=0.4 W as the single soliton threshold and then use the single soliton critical product condition $T_0^2|u_0|^2\times10^4=86$ ns^2 to estimate a power scaling factor. One obtains a power scaling factor $|u_0|^2\times10^4/P_{in}=[(86/10^2)/0.4\ \text{W}]=2.2\ \text{W}^{-1}$. In Ref. 14, however, this condition was coupled with an additional association for the point at which the output peak power versus input peak power data exhibited a peak. The data in Fig. 7 show no peak, but only indicate the possibility of a peak at some value of P_{in} in excess of 3 W. If, following Ref. 14, one assumes that a peak in P_{out} vs P_{in} should occur at the point in input peak power for which the condition $T_n=T_p$ is satisfied, the scaling factor obtained above yields an expected peak position at $P_{in}\approx5.3$ W. Such a peak, at least, is not inconsistent with the data.

It is useful at this point to consider the results in Figs. 6 and 7 in terms of the various characteristic times and critical product soliton thresholds established in Sec. II. First of all, the input pulse width $T_0=10$ ns translates into a characteristic dispersion time $T_d\approx930$ ns. This means that on the time scale of the measurements, with a propagation time $T_p\approx90$ ns, one should see no dispersion effects. This expectation is supported by the trace (a) profiles in Fig. 6. The output pulse, while not square, still has about the same width as the input pulse.

Second, consider the characteristic nonlinear-response times associated with the results shown above. The working equation in Table I, $T_n=1020/|u_0|^2\times10^4$, in combination with the power scaling factor $|u_0|^2\times10^4/P_{in}=2.2\ \text{W}^{-1}$, translates into a nonlinear-response time T_n(ns) $\approx[460/P_{in}(\text{W})]$. As far as the results in Figs. 6 and 7 are concerned, this means that T_n is decreasing as the input peak power P_{in} is increasing. Based on the parameters given above, T_n does not drop below the propagation time $T_p\approx90$ ns until the input peak power exceeds about 5 W. It is clear, therefore, that the evolution of pulse shapes shown in Fig. 6 and the output peak power versus input peak power data in Fig. 7 correspond to a situation in which the soliton forma-

tion time is continuously decreasing but is always greater than the propagation time. At the $P_{in} \approx 3$ W limit for the experiment, the nonlinear-response time is about 150 ns, still 50% greater than the propagation time. This means that a simple interpretation of the peaks in Fig. 6 or the data in Fig. 7 in terms of soliton thresholds is difficult as best.

Consider, for example, the expected thresholds based on the power scaling factor established above and the observed response above these thresholds. That power scaling factor, the $T_0 = 10$ ns input pulse width, and the critical product recipe in Sec. III give threshold P_{in} values of 0.4, 3.5, and 9.8 W, respectively, for $n=1$, $n=2$, and $n=3$ solitons. For $n=1$, the threshold power of 0.4 W was, of course, the basis for the power scaling in the first place. At $P_{in}=0.4$ W, however, the nonlinear-response time T_n is 1150 ns and still well above the propagation time. This means that the increase in the observed P_{out}, as P_{in} increases above 0.4 W, corresponds to the soliton very early in its formation process. The actual increase is due to a combination of two factors, the increasing power and the decreasing nonlinear-response time T_n.

Apart from these considerations for the $n=1$ single soliton case, there are no clear one-to-one correlations between the features in the Fig. 6 and Fig. 7 data and the soliton threshold powers listed above for more than one soliton. The estimated threshold power for two solitons is just at the limit of the power available in the experiment. The second peak evident in Fig. 6 may be due to a second soliton. The estimated threshold power for three solitons is well above the maximum power in the experiment. There are no clear multiple soliton effects evident from Fig. 7.

B. Experiments for constant input pulse power

In the second set of experiments, the input peak power level was held constant while the input pulse width was increased. A representative set of input and output pulse profiles for this procedure is shown in Fig. 8. Traces (a)–(f) show measured power input and output pulse profiles for input pulses with widths of 4, 10, 17, 26, 36, and 48 ns, respectively, at a peak power level of approximately 2 W. Here, as in Fig. 6, the power scales for the input pulses are in watts, while the power scales for the output pulses are in milliwatts. Note also that the propagation time for all power levels is about 90 ns, the same as before.

Trace (a) in Fig. 8, for an input pulse width of 4 ns, shows no pulse steepening or narrowing. At this width, the response is in the linear, dispersive region. The dashed line shows the output profile expanded by a factor of 5 on the power scale. The output is broad and somewhat wider than the input pulse. When the pulse width is increased to 10 ns, as shown in trace (b), one sees the steepening and narrowing which is characteristic of soliton formation. Trace (b), moreover, corresponds directly to trace (c) in Fig. 6. When the input pulse width is further increased to 17 ns, as in trace (c), the initial soliton output pulse is almost unchanged and one sees the formation of a second pulse. With the further increase of the input pulse width, a three peak MME soliton pulse is formed at 26 ns and a four peak pulse is formed at 36 ns, as shown by traces (d) and (e), respectively. In the case of even longer pulses, as shown by trace (f) for 48 ns, the multiple peaks may no longer be clearly distinguished. Note also that as the pulse width increases, the first soliton peak, once formed, undergoes only small changes and basically remains the same.

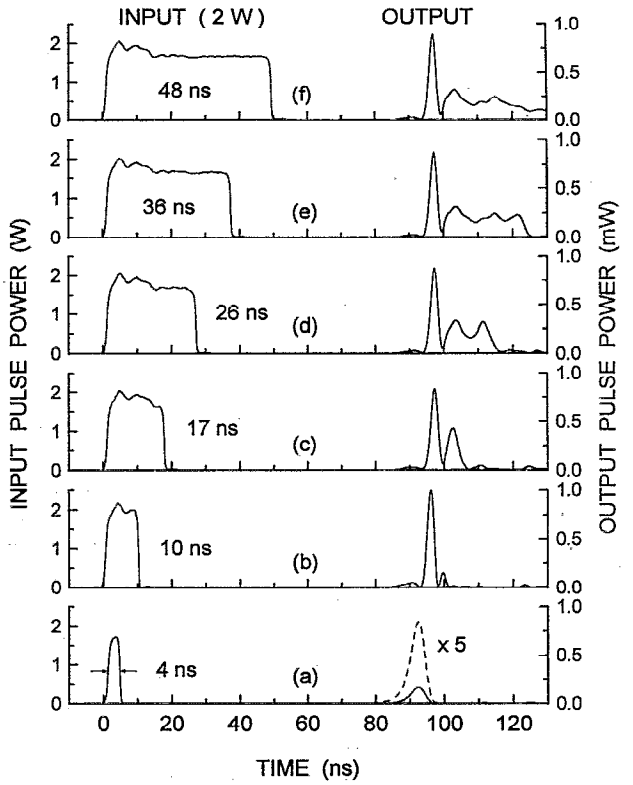

FIG. 8. Input and output profiles of detected power vs time for the YIG film transducer structure of Fig. 1 in the MSFVW configuration for the six different input pulse widths indicated. The film thickness was 7.2 μm and the external applied field was 3744 Oe. The carrier frequency was 5.6 GHz and the input pulse peak power was held constant at 2 W. The dashed curve for output profile (a) shows the pulse with the vertical response expanded by a factor of 5.

In parallel with the P_{out} vs P_{in} measurements for a fixed pulse width, a useful follow up to the pulse profiles in Fig. 8 is to measure the dependence of the output peak power P_{out} on the input pulse width T_0 at fixed input power. Figure 9 shows the results of such measurements carried out at an input power level of 2 W, the same as for the pulse profiles in Fig. 8. The filled circles represent the data. The solid lines connect the data points. The initial increase of output peak power with increasing input pulse width when T_0 is small is due mainly to the decreasing influence of the dispersion as the pulses widen and their frequency spectrum narrows. The rate of increase in P_{out} with T_0 becomes more rapid for T_0 in the 5–10 ns range. The measured P_{out} reaches a peak near $T_0 = 12$ ns, decreases, and then levels off for pulse widths above 15–20 ns or so.

The data in Fig. 9 reflect the basic trends shown by the actual pulse profiles in Fig. 8. As was done for the constant input pulse width measurements, it is useful to consider the Fig. 8 and Fig. 9 results in terms of the applicable characteristic times and threshold conditions. Based on the power scale factor of 2.2 W^{-1}, the $P_{in}=2$ W condition applicable to

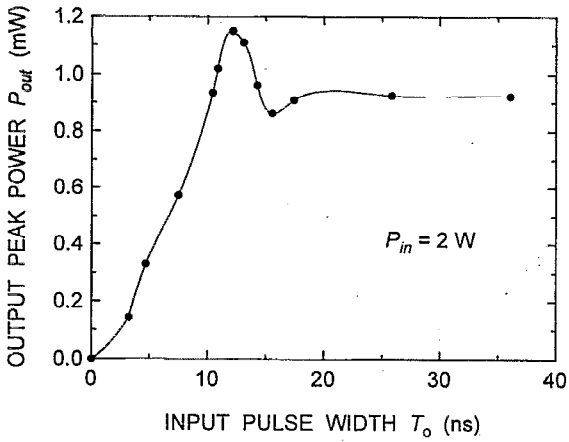

FIG. 9. Measurements of output peak power P_{out} vs input pulse width T_0 for a series of pulse propagation experiments with the YIG film transducer structure of Fig. 1 in the MSFVW configuration and with the input pulse peak power P_{in} held constant at 2 W. The film thickness was 7.2 μm and the external applied field was 3744 Oe. The carrier frequency was 5.6 GHz. The solid circle data points are connected by a smooth curve.

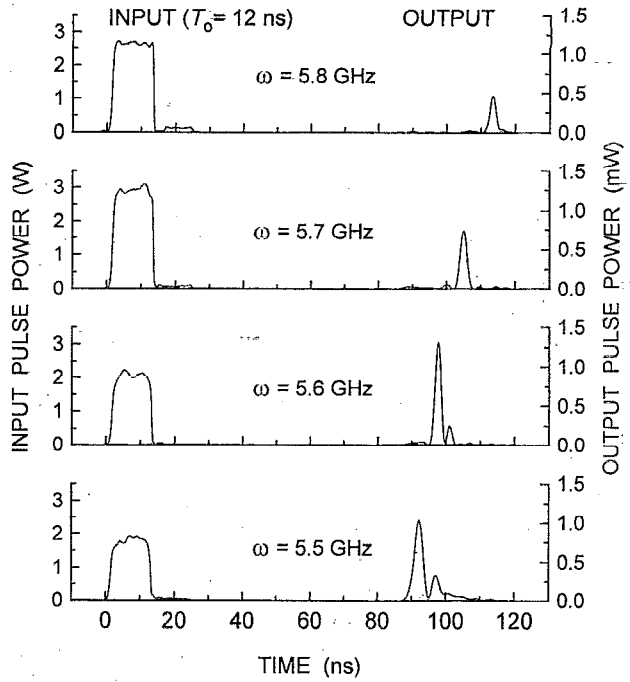

FIG. 10. Input and output profiles of detected power vs time for the YIG film transducer structure of Fig. 1 in the MSFVW configuration for the four different carrier frequencies indicated. The input pulse width T_0 was held constant at 12 ns. The film thickness was 7.2 μm and the external applied field was 3744 Oe.

Figs. 8 and 9 gives a $|u_0|^2\times10^4$ value of 4.4. This power amplitude gives a nonlinear-response time $T_n\approx230$ ns, more than a factor of 2 longer than the propagation time at the point of detection, $T_p\approx90$ ns. This means that for $P_{in}=2$ W, one is always *below* the power level for the detection of fully formed solitons at the output transducer.

This $|u_0|^2\times10^4$ value of 4.4 may also be combined with the critical product condition to obtain threshold input pulse widths for $n=1$, $n=2$, etc., solitons. One obtains a single soliton threshold pulse width of about 5 ns, a two soliton threshold width of 13 ns, a three soliton threshold of 22 ns, etc. The single soliton threshold time of 5 ns matches, more or less, the appearance of a soliton pulse at $T_0=10$ ns as shown in Fig. 8 and the increase in the P_{out} vs T_0 rate of response in the 5–10 ns range in Fig. 9. The 13 and 22 ns widths also match, more or less, the two peaked and three peaked profiles in Fig. 8 and the features in Fig. 9. As in the fixed pulse width results, one does not expect to see pronounced soliton threshold effects. As already indicated, the measurements correspond to solitons quite early in their formation process.

C. Solitons at different frequencies

An important parameter for possible MME soliton device applications is bandwidth, or the range of frequencies within the MSW band for which soliton pulses can be launched and detected. The work discussed above was for a frequency of 5.6 GHz, 200 MHz above the bottom of the MSFVW band. The question of interest here is soliton propagation at higher frequencies. The ultimate limit is the top of the MSFVW band at ω_B. As already indicated, this cutoff in the present situation is at about 7.5 GHz. As shown in Fig. 4 and discussed above, however, the useful range of frequencies is only from 5.4 to about 6 GHz. Above 6 GHz, the low values of the group velocity v_g and the weak stripline coupling to the high k modes lead to a high transmission loss and essentially no usable signal. The purpose of the measurements presented below is to demonstrate that soliton pulses can be obtained over the entire useful MSFVW passband from 5.4 to 6 GHz.

Figure 10 shows the results of the experiments carried out at various frequencies within the useful MSFVW passband. As before, the static external magnetic field of 3744 Oe was maintained constant and perpendicular to the film plane for all measurements. Four traces are shown in Fig. 10, for carrier frequencies of 5.5, 5.6, 5.7, and 5.8 GHz. The input pulse width T_0 was held constant at 12 ns. The input peak powers ranged between 2 and 3 W. It was necessary to increase the peak power somewhat as the frequency was increased to compensate for the increase in transmission loss evident from Fig. 4. The differences in the amplitude and shapes of the soliton output pulses are due mainly to the increase in transmission loss with frequency. The propagation times are essentially the same as indicated in Fig. 5. All of the output pulses in Fig. 10 have sharp profiles which are similar to the output profiles in Figs. 6 and 8, and may be taken to represent solitons. These results show that one can produce soliton pulses over the entire useful MSFVW passband.

The basic comparisons of Secs. IV A and IV B, in terms of characteristic times and critical products, apply here. One must, however, be careful to take into account the changes in the group velocity v_g, the dispersion parameter ω_k'', and the N parameter with frequency. Recall that the N parameter specified by Eq. (10) corresponds to $\omega_k=\omega_H$. If one takes these changes into account, and keeps the power scale factor at 2.2 W^{-1}, one obtains nonlinear-response times which

range from 260 ns at 5.5 GHz to 180 ns at 5.8 GHz. The corresponding propagation times range from 90 to 110 ns. This means that, as for the 5.6 GHz results, the soliton pulses at detection are not fully developed. The 5.6 GHz power scale factor of 2.2 W^{-1} gives a single soliton power threshold at $T_0=12$ ns which ranges from 0.44 W at 5.5 GHz to 0.33 W at 5.8 GHz. These thresholds are well below the P_{in} values shown in Fig. 10. One also needs to keep in mind the fact that the wave number of the MSFVW carrier signal is increasing with frequency and the coupling between the input transducer and the film is decreasing. This will cause the power scaling factor to decrease with increasing frequency and increase the soliton power thresholds.

The trend of the output pulse amplitude to decrease as the frequency increases is due to a combination of factors. The main factor is in the rapidly decreasing group velocity and the corresponding decay in the amplitude of the propagating pulse due to relaxation. In addition to the direct effect on output signal, this decay in amplitude can also push the pulse out of the soliton regime and back into the linear regime. Furthermore, the changes in the characteristic times, critical power levels, and the power scaling factor with frequency affect the amplitude of the detected soliton pulse. The interplay of factors here is clearly complicated.

D. Soliton propagation loss

This section on experimental results is concluded with a different type of measurement. This measurement is based on the ability to launch MME pulses at the input transducer and detect the pulses as they pass the pickup transducer, as before, but then allow these forward traveling pulses to reflect off the end of the YIG film strip and be detected a second time as they travel back in the reverse direction. In order to achieve a reasonable reflection coefficient, the YIG strip with tapered ends, as shown in Fig. 1, was replaced by a YIG strip with a square end and carefully prepared edges. Two types of experiments were carried out, one with single pulses and one with two pulses. The results below are from the single pulse experiments. The two pulse experiments are considered in Sec. IV E.

In the single pulse edge reflection experiments, MME pulses were launched and then detected by the pickup transducer during the forward and backward traveling passes for the pulse. As the distance between the pickup transducer and the reflecting end was changed, the propagation time was also changed. It was then possible, from measurements of the detected pulse amplitudes for the two passes, to determine decay attenuation rates and relaxation times for the propagating MME pulses. Such measurements were carried out as a function of pulse width at low power and for relatively short pulse widths at high power. The low power measurements provided a determination of both the reflection loss and the low power attenuation rate. The high power measurements provided additional information on soliton decay.

It is to be recalled that single soliton pulses are expected to decay at twice the rate for linear pulses. This result was considered in Sec. II and shown in Eq. (11). This double decay rate prediction was first confirmed by Kalinikos and co-workers[16] on the basis of experiments with a structure similar to the one in Fig. 1, but with the capability to vary the spacing between the input and output transducers. In the high power, soliton regime, the attenuation in the detected pulse amplitude as a function of propagation distance had a slope which was approximately twice the linear attenuation rate estimated from phenomenological propagation loss theory.[32] The approach here accomplishes the same objective of a variable propagation distance in a different way, by detecting the pulse two times, once before and once after reflection from the end of the film.

For these experiments, a slightly shorter YIG film strip, 2 mm×12.5 mm in size, was used. The strip had squared off rather than tapered ends and carefully prepared edges. Efficient reflection of MSW pulses at the film edge occurs because of the sharp decrease of the demagnetizing field at such edges.[33] This causes the net internal field to increase and pushes the MSFVW band up in frequency and well above the operating point. Under such conditions, the edge region of the film does not support forward volume waves and the edge itself becomes a very good reflector. One may then use the positioning of the YIG strip relative to the pickup transducer to achieve a variable round trip propagation length for the pulse. For the results given below, the distance between the receiving transducer and the reflecting edge of the film strip ranged from about 2 to 4 mm. The experiments were carried out at the 5.6 GHz operating point, with the same static field used above. Propagation times ranged from 90 to 180 ns.

The basic measurement here consists of two detected peak power values, P_F for initial pass of the pulse and P_R for the reverse traveling pulse after reflection, and the round trip propagation time between the peak power measurements, T_T. The overall attenuation in decibels will be given by $\Gamma(\mathrm{dB})=10\log(P_F/P_R)$. This $\Gamma(\mathrm{dB})$ will contain two parts. One part, $\Gamma_E(\mathrm{dB})$, will come from losses connected with the edge reflection. The second part, specified as $A(\mathrm{dB}/\mu s)T_T(\mu s)$, will be associated with the physical relaxation rate for the propagating MME wave packet in the YIG strip

$$\Gamma(\mathrm{dB})=\Gamma_E(\mathrm{dB})+A(\mathrm{dB}/\mu s)T_T. \tag{19}$$

The attenuation rate parameter A, expressed in dB/μs, may be obtained from Eq. (19). A is directly related to the relaxation rate η_A for the propagating MME signal. One may write operational equations for these parameters as follows:

$$A(\mathrm{dB}/\mu s)=\frac{1}{T_T}\left[10\log\frac{P_F}{P_R}-\Gamma_E(\mathrm{dB})\right], \tag{20}$$

$$\eta_A(\mathrm{rad/s})=\frac{5\times10^4}{\log e}A(\mathrm{dB}/\mu s). \tag{21}$$

Note that η_A is the exponential decay rate for the normalized dynamic magnetization response function $u(x,t)$ introduced in Sec. II. The decay rate for power is twice this value. Based on the discussion of Sec. II, one would expect A and η_A values which correspond to the intrinsic relaxation rate η for very wide, low power pulses. The observed attenuation rate would be larger for narrow, low power pulses because of dispersion spreading. In the high power soliton regime, one

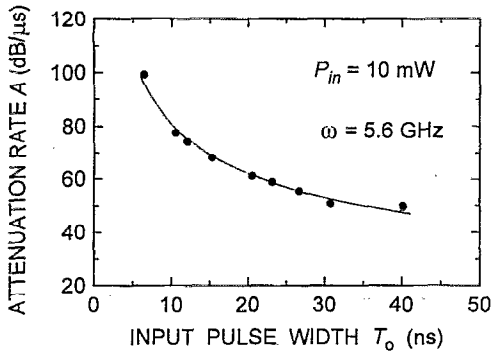

FIG. 11. Experimental values of the attenuation rate A, in dB/μs, vs input pulse width T_0 for low power MSFVW pulses propagated in the YIG film transducer structure of Fig. 1. The pulses were launched from the input transducer, detected by the output transducer, reflected from the end edge of the film, and then detected a second time. The input peak power was 10 mW, the external applied field was 3744 Oe, and the carrier frequency was 5.6 GHz. The solid circles show the data. The solid line represents a fitted curve to the data.

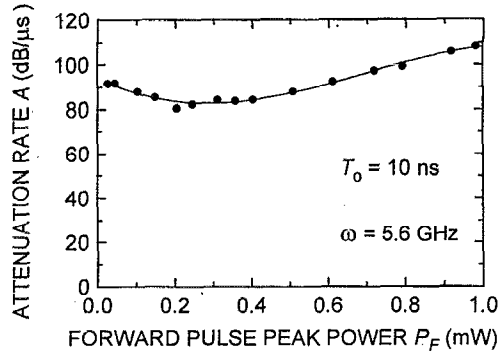

FIG. 12. Experimental values of the attenuation rate A, in dB/μs, vs the initial detected peak power for the forward traveling pulse P_F for high power MSFVW pulses propagated in the YIG film transducer structure of Fig. 1. The pulses were launched from the input transducer, detected by the output transducer, reflected from the end edge of the film, and then detected a second time. The input pulse width was 10 ns, the external applied field was 3744 Oe, and the carrier frequency was 5.6 GHz. The solid circles show the data. The solid line represents a fitted curve to the data.

would expect A and η_A values which correspond to a relaxation rate of 2η. The experiments described below confirm these expectations.

Measurements were first carried out at low input power levels in the 10 mW range. Two separate experiments were done. First, data on the total attenuation Γ as a function of the round trip propagation time T_T for relatively wide, 50 ns pulses were obtained. The attenuation was found to be a linear function of the propagation time. The data yielded an attenuation rate $A=53\pm10$ dB/μs and an edge reflection loss $\Gamma_E=0.5\pm0.5$ dB. The edge attenuation loss is seen to be quite small. Edge attenuation has little effect on the overall attenuation values.

Attenuation measurements were then made as a function of input pulse width for a fixed propagation time of about 90 ns. Representative data on the attenuation rate A as a function of input pulse width T_0 are shown in Fig. 11. Measured values are shown by the solid circles. The solid curve represents a smooth curve fit to the data. The results in Fig. 11 show that the attenuation rate is quite large when the pulse width is small and decreases asymptotically to some limiting value as T_0 increases beyond 40–50 ns or so. Recall that the overall propagation times are on the order of 100–200 ns and the characteristic dispersion times from Sec. II are on the order of 9.3 $[T_0(\text{ns})]^2(\text{ns})$. At $T_0=40-50$ ns, the dispersion time T_d is a factor of 100 or so greater than such propagation times. In this limit, the attenuation rate A value is about 40–50 dB/μs. The corresponding relaxation rate from Eq. (21) is 5.2×10^6 rad/s. This value of η_A corresponds to a ferromagnetic-resonance derivative linewidth of 0.34 Oe and is very close to the value for the YIG relaxation rate used in Ref. 14. This value will be taken, therefore, as the applicable relaxation rate for low power MSFVW pulse propagation in YIG. This is the value cited in Sec. II and listed in Table I.

Turn now to the high power attenuation measurements. In these experiments, the attenuation rate A was determined as a function of the peak power P_F for the forward traveling pulse. The pulses were initially generated from input pulses which were 10 ns in width and had peak power values in the range shown in Fig. 7. These conditions were selected for easy reference to the results presented in Fig. 6 and Fig. 7. The results of these measurements are shown in Fig. 12. The solid circles are the measured points and the curve represents a fit to the data. Note that the independent variable plotted on the horizontal axis is the forward traveling pulse peak power value P_F, and that the range of these P_F values is 0–1 mW. This range matches the lower two-thirds of the range of P_{out} values shown in Fig. 7. It corresponds to the range of input peak powers over which the output pulses transform from the linear regime to the soliton regime.

Overall, the attenuation rate values shown in Fig. 12 are significantly larger than the values shown in Fig. 11. The 90 dB/μs values for A at the very low values of P_F are on the same order as the low power A values for $T_0\approx10$ ns in Fig. 11. These large attenuation rates are due to dispersion effects at low power for such narrow pulses. As P_F is increased, however, the attenuation rate shows a small but distinct decrease, goes through a shallow minimum at $P_F\approx0.3$ mW or so, and then slowly increases at higher P_F values. The decrease can be attributed to soliton formation. Note that soliton formation is expected, on the basis of the results in Fig. 7, for P_F values above 0.05 mW or so. The immediate decrease in the attenuation rate as P_F is increased from the lowest values is consistent with this observation.

The minimum at $P_F\approx0.3$ mW and the increase in A at higher powers is also consistent with soliton considerations. The key result in Fig. 12 is in the values of the attenuation rate A for $P_F>0.3$ mW. These values are approximately double the attenuation rate in the low power regime for wide pulses. This double attenuation rate indicates that the effective relaxation rate has also doubled. Such a doubling, moreover, is expected for solitons. That expectation was discussed in detail in Sec. II and indicated in Eq. (11).

E. Soliton collisions

Although the narrowing and steepening of the output pulse profiles shown in Figs. 6 and 8 are important indicators

for soliton formation, a key property of solitons in general is their ability to pass through one another unchanged.[34] The edge reflection technique, described above in connection with attenuation measurements, provides a convenient way to observe solitons before and after interaction with other solitons. The purpose of this section is to present some qualitative results on MSFVW solitons in collision based on this technique.

The collision experiments followed the same procedure described above. Soliton pulses were launched from the input transducer. They were first detected by the pickup transducer during their forward traveling pass approximately 90 ns after launch, allowed to reflect off the end edge of the YIG strip, and then detected a second time while traveling back from the edge in the reverse direction. In order to obtain conditions for soliton collision, two pulses were launched instead of one, with an appropriate time delay between the two pulses. If this time delay is less than the round trip propagation time T_T, the first soliton pulse will have passed through the second soliton pulse during its backward traveling pass and prior to the second detection.

These specific pulse collision experiments used the same film as used for the attenuation measurements. The YIG strip was positioned with the reflecting edge approximately 2 mm from the pickup transducer. The static magnetic field was the same as before. The 2 mm spacing and lower frequency gave an input transducer to pickup transducer propagation time of about 88 ns, and a pickup transducer to film edge and return round trip propagation time of about 87 ns. The time delay between the two input pulses was set at 40 ns. The experiments were done for 10 ns wide input pulses. Single pulse and double pulse measurements were carried out under both low and high input peak power conditions. The low power case used pulses with $P_{in} \approx 0.1$ W, well below the soliton regime. The high power case used pulses with $P_{in} \approx 1.8$ W, well above the single soliton threshold.

The carrier frequency was 5.52 GHz, slightly lower than the 5.6 GHz value used for most of the other experiments described above. This fine tuning in frequency was necessary to optimize the size of the detected output signals. As evident from Figs. 4 and 5, one can have wide variations in the actual transmission loss and propagation times for very small changes in frequency because of the exchange gap effects associated with residual pinning. In these experiments, it is important to optimize the transmission in order to obtain a sufficient signal for detection after the edge reflection and additional propagation distance. For this reason, the frequency operating point was fine tuned to 5.52 GHz to achieve the maximum signal.

Representative results are shown in Fig. 13. The first and second input pulses are labeled as I_1 and I_2, respectively. The forward pass pickup signals for these inputs are labeled as F_1 and F_2, and the reverse pass pickup signals after reflection are labeled as R_1 and R_2. Traces (a) and (b) are for single and double low power pulses and traces (c) and (d) are for single and double pulses at high power. The signals at 5 and 45 ns represent the input pulses, with the corresponding power scales in watts along the left-hand vertical axes. The forward pass signal peaks are at 90 and 130 ns. The edge

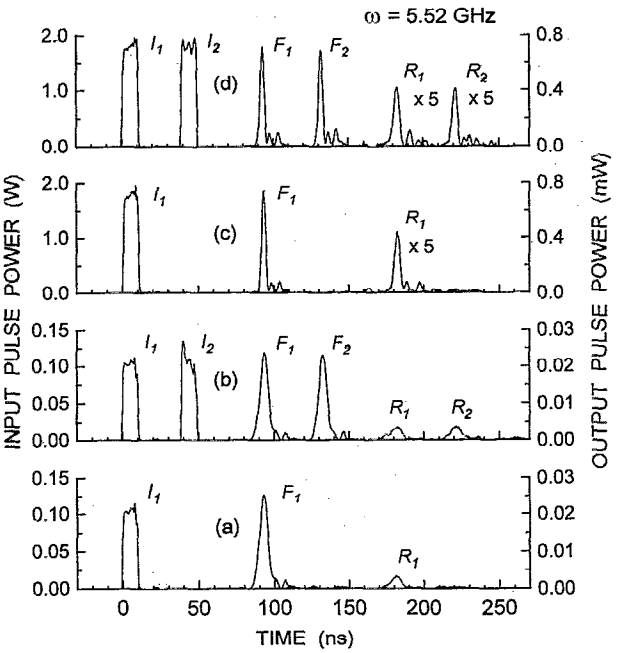

FIG. 13. Input and output profiles of detected power vs time for the YIG film transducer structure of Fig. 1 in the MSFVW configuration for four different YIG film end edge reflection experiments. The film thickness was 7.2 μm and the external applied field was 3744 Oe. The carrier frequency was 5.52 GHz and the input pulse width was 10 ns. The input peak power was 0.1 W for traces (a) and (b) and 1.8 W for traces (c) and (d). Single pulses were used for traces (a) and (c), and two pulses delayed by 40 ns were used for traces (b) and (d). The labels I_1 and I_2 denote the first and second input pulses, respectively. The labels F_1 and F_2 denote the corresponding signals at the output transducer for the forward traveling pulses, detected approximately 87 ns after launch. The labels R_1 and R_2 denote the corresponding signals at the output transducer for the same pulses after reflection off the end edge of the YIG film, detected approximately 180 ns after launch. The curves for profiles R_1 and R_2 in traces (c) and (d) have vertical scales which are expanded by a factor of 5.

reflected reverse pass signal peaks are at 180 and 220 ns. The pickup power scales, in milliwatts, are on the right-hand vertical axes.

Consider first the low power results. For the single pulse case shown in trace (a), the round trip propagation causes the F_1 profile at 90 ns to decay in amplitude and spread in width to yield the R_1 profile shown at 180 ns. The peak power drops by about a factor of 8, which corresponds to a decay rate of 103 dB/μs. Trace (b) shows the effect of adding the second pulse. The situation is about the same as in trace (a), except that there are now two forward pass and two reverse pass signals. The decay and spreading is about the same for the second pulse as for the first pulse.

Turn now to the high power results. Note that the R_1 and R_2 profiles have vertical scales which are expanded by a factor of 5. The F_1 and R_1 profiles for the single pulse case in trace (c) show clear soliton properties. These profiles are sharp and narrow. Even though the R_1 profile appears to be slightly wider than the F_1 profile, both are still significantly narrower than the input pulse. The decay in peak power from the F_1 profile to the R_1 profile is by a factor of 8.3. This corresponds to a decay rate of about 105 dB/μs.

Trace (d) in Fig. 13 shows representative results for two input pulses at high power. Here, instead of one forward pass and one reverse pass soliton profile, there are two forward pass and two reverse pass soliton peaks. The timing is such that the first soliton pulse and the second soliton pulse have passed through each other prior to producing the signals shown by the R_1 and R_2 profiles in trace (d). These experiments show, therefore, that two MSFVW MME solitons can pass through each other without modifying the pulse shapes or the propagation speed for either signal.

The attenuation rates for the signals in Fig. 13 are consistent with the decay rates presented in the previous section. The low power decay rate of 103 dB/μs is on the order of the decay rates in Fig. 11 in the limit of short pulses. This rate is large because of the effect of dispersion for the short 10 ns pulses. The high power decay rate of 105 dB/μs is about the same as in Fig. 12. This rate is large, not because of dispersion, but because of the doubling in the relaxation rate for solitons.

The soliton collision results presented above represent a first step in the investigation of the interaction of microwave magnetic envelope solitons in thin films. Experiments are in progress to use precision propagation time measurements to study soliton interactions in detail. It is expected, for example, that the close range interaction between solitons can be attractive or repulsive, depending on the relative carrier phases for the pulses.[5] Such interactions may be extremely important, not only for the basic understanding of soliton properties, but also because of the sequential effect of collision induced phase shifts on multiple soliton data packets.[35]

V. CONCLUSION

The above sections have presented a fairly complete set of experiments and analyses on both the linear and the nonlinear response for magnetostatic forward volume wave pulses at 5.5–6.0 GHz in YIG films. The experiments utilized a magnetostatic wave transducer structure with a narrow linewidth single-crystal YIG film. At low power, one obtains well-known MSFVW pulse propagation and attenuation characteristics. At high power, one obtains nonlinear effects in the narrowing and steepening of pulse shapes, the appearance of multiple peaks in the detected pulse, and peak power profiles which show many characteristics associated with envelope solitons. The connection between the experimental results and soliton processes is then considered in terms of various characteristic times for linear and nonlinear MSW wave packets. Good consistency is obtained. It was possible to generate and detect such solitons over the entire low attenuation range of the MSFVW band. Finally, careful measurements of both forward traveling and edge reflected reverse traveling pulses are used to determine the decay and attenuation and decay properties of linear and nonlinear pulses, and to observe the effects of pulse collisions. It is found that the decay rates for MME pulses in the soliton regime are approximately twice the decay rates for low power pulses, in accord with theory. It is also found that pulses in the nonlinear soliton regime are able to pass through each other intact, with little change in shape or speed.

ACKNOWLEDGMENTS

The authors gratefully acknowledge Dr. J. D. Adam of the Westinghouse Research and Development Center, Pittsburgh, Pennsylvania for providing the YIG films for the experiment. The authors also thank Dr. M. J. Ablowitz, Dr. A. D. Boardman, Dr. S. Chakravarty, Dr. P. Kabos, Dr. B. A. Kalinikos, Dr. L. F. Mollenauer, Dr. S. A. Nikitov, and Dr. A. N. Slavin for helpful discussions. This work was supported in part by the National Science Foundation under Grant Nos. DMR-8921761 and DMR 9400276, and by the U. S. Army Research Office under Grant No. DAAL03-91-G-0327.

[1] A. Hasegawa and F. Tappert, Appl. Phys. Lett. **23**, 142 (1973); A. Hasegawa and F. Tappert, *ibid.* **23**, 171 (1973).
[2] L. F. Mollenauer, R. H. Stolen, and J. P. Gordon, Phys. Rev. Lett. **45**, 1095 (1980).
[3] L. F. Mollenauer and K. Smith, Opt. Lett. **13**, 675 (1988).
[4] A. Hasegawa, *Optical Solitons in Fibers*, 2nd ed. (Springer, Berlin, 1990).
[5] H. A. Haus, IEEE Spectrum **30**, 48 (1993).
[6] E. Desurvire, Phys. Today **47** (No. 1), 20 (1994).
[7] B. A. Kalinikos, N. G. Kovshikov, and A. N. Slavin, Pis'ma Zh. Eksp. Teor. Fiz. **38**, 343 (1983) [JETP Lett. **38**, 413 (1983)].
[8] B. A. Kalinikos, N. G. Kovshikov, and A. N. Slavin, IEEE Trans. Magn. **26**, 1477 (1990).
[9] B. A. Kalinikos, N. G. Kovshikov, and A. N. Slavin, Phys. Rev. B **42**, 8658 (1990).
[10] P. De Gasperis, R. Marcelli, and G. Miccoli, Phys. Rev. Lett. **59**, 481 (1987).
[11] P. De Gasperis, R. Marcelli, and G. Miccoli, J. Appl. Phys. **63**, 4136 (1988).
[12] B. A. Kalinikos, N. G. Kovshikov, P. A. Kolodin, and A. N. Slavin, Solid State Commun. **74**, 989 (1990).
[13] M. Chen, M. A. Tsankov, J. M. Nash, and C. E. Patton, J. Appl. Phys. **74**, 2146 (1993).
[14] M. Chen, M. A. Tsankov, J. M. Nash, and C. E. Patton, Phys. Rev. B **49**, 12773 (1994).
[15] M. Chen, M. A. Tsankov, J. M. Nash, and C. E. Patton, Phys. Rev. Lett. **70**, 1707 (1993).
[16] A. Kalinikos, N. G. Kovshikov, and A. N. Slavin, IEEE Trans. Magn. **28**, 3207 (1992).
[17] V. E. Zakharov and A. B. Shabat, Zh. Eksp. Teor. Fiz. **61**, 118 (1971) [Sov. Phys. JETP **34**, 62 (1972)].
[18] V. E. Zakharov and A. B. Shabat, Zh. Eksp. Teor. Fiz. **64**, 1627 (1973) [Sov. Phys. JETP **37**, 823 (1973)].
[19] V. P. Lukomskii, Ukr. Fiz. Zh. **23**, 134 (1978).
[20] A. K. Zvezdin and A. F. Popkov, Zh. Eksp. Teor. Fiz. **84**, 606 (1983) [Sov. Phys. JETP **57**, 350 (1983)].
[21] G. P. Agrawal, *Nonlinear Fiber Optics* (Academic, Boston, 1989).
[22] R. W. Damon and H. van de Vaart, J. Appl. Phys. **36**, 3453 (1965).
[23] J. D. Adam, M. R. Daniel, P. R. Emtage, and S. H. Talisa, in *Physics of Thin Films*, edited by M. H. Francombe and J. L. Vossen (Academic, Boston, 1991), Vol. 15, p. 2, and references therein.
[24] B. A. Kalinikos and A. N. Slavin, J. Phys. C **19**, 7013 (1986).
[25] M. J. Lighthill, J. Inst. Math. Appl. **1**, 269 (1965).
[26] G. L. Lamb, *Elements of Soliton Theory* (Wiley, New York, 1980).
[27] Y. Kodama and M. J. Ablowitz, Stud. Appl. Math. **64**, 225 (1981).
[28] H. Suhl, J. Phys. Chem. Solids **1**, 209 (1957).
[29] J. D. Adam, T. W. O'Keeffe, and R. W. Patterson, J. Appl. Phys. **50**, 2446 (1979).
[30] J. D. Adam, Circuits Syst. Signal Process. **4**, 105 (1985).
[31] J. M. Nash, M. Chen, M. A. Tsankov, and C. E. Patton, J. Appl. Phys. **75**, 5629 (1994).
[32] D. D. Stancil, J. Appl. Phys. **59**, 218 (1986).
[33] R. I. Joseph and E. Schlömann, J. Appl. Phys. **36**, 1579 (1965).
[34] A. C. Scott, F. Y. F. Chu, and D. W. McLaughlin, Proc. IEEE **61**, 1443 (1973).
[35] A. F. Benner, J. R. Sauer, and M. J. Ablowitz, J. Opt. Soc. Am. B **10**, 2331 (1993).